

## Article

# A Study of the Dusty Disks and Shells around Post-RGB Stars in the LMC

Geetanjali Sarkar <sup>1,\*</sup>  and Raghvendra Sahai <sup>2</sup> <sup>1</sup> Department of Physics, Indian Institute of Technology, Kanpur 208016, India<sup>2</sup> Jet Propulsion Laboratory, California Institute of Technology, 4800 Oak Grove Drive, Pasadena, CA 91109, USA; raghvendra.sahai@jpl.nasa.gov

\* Correspondence: gsarkar@iitk.ac.in

**Abstract:** A new class of dusty post-Red Giant Branch (post-RGB) stars has recently been identified in the Magellanic Clouds. Their spectral energy distributions (SEDs) suggest that their mass-ejecta are similar to dusty post-Asymptotic Giant Branch (post-AGB) stars. We modeled the SEDs of a select sample of post-RGB and post-AGB stars in the Large Magellanic Cloud (LMC), quantified the total dust mass in the disks and shells and set rough constraints on the dust grain compositions and sizes. The shells were significantly more massive than the disks. Our models suggest that circumstellar disks, when present, are geometrically thick with a substantial opening angle, which is consistent with numerical simulations of CE evolution (CEE). Comparison of our model dust mass values with the predictions of dust production during CEE on the RGB suggest that CEE occurred near or at the tip of the RGB for the post-RGB sources in our sample. Amorphous silicate emission features at 10 and 18  $\mu\text{m}$  are seen in the model spectra of several post-RGBs. A surprising result is that the ejected dust in certain post-RGB sources appears to be carbon-rich, thus, providing independent support for the hypothesis of binary interactions leading to the formation of dusty post-RGB objects.



**Citation:** Sarkar, G.; Sahai, R. A Study of the Dusty Disks and Shells around Post-RGB Stars in the LMC. *Galaxies* **2022**, *10*, 56. <https://doi.org/10.3390/galaxies10020056>

Academic Editors: Martín Guerrero, Noam Soker and Quentin A. Parker

Received: 1 February 2022

Accepted: 17 March 2022

Published: 2 April 2022

**Publisher's Note:** MDPI stays neutral with regard to jurisdictional claims in published maps and institutional affiliations.



**Copyright:** © 2022 by the authors. Licensee MDPI, Basel, Switzerland. This article is an open access article distributed under the terms and conditions of the Creative Commons Attribution (CC BY) license (<https://creativecommons.org/licenses/by/4.0/>).

**Keywords:** circumstellar dust; evolved stars; Red Giant Stars; post-Asymptotic Giant Branch stars; (stars:) binaries

## 1. Introduction

Collimated bipolar lobes separated by a dusty disk or torus are the hallmark of protoplanetary nebulae (PPNs)—objects in transition between the Asymptotic Giant Branch (AGB) and Planetary Nebula (PN) evolutionary phases (Bujarrabal et al. [1]; García-Lario, Riera & Manchado [2]; Hrivnak et al. 2008 [3]; Kwok, Su & Hrivnak [4]; Kwok, Hrivnak & Su [5]; Sahai et al. [6]). The very luminous (a few  $10^3$  to a few  $10^4 \text{ L}_\odot$ ), cool ( $T_{\text{eff}} < 3000 \text{ K}$ ) AGB phase is characterised by heavy mass-loss (with rates as high as  $10^{-4} \text{ M}_\odot \text{ yr}^{-1}$ ).

After mass-loss has depleted most of the stellar envelope, the stars evolve to higher temperatures through the post-AGB phase at almost constant luminosity. The largely spherical (AGB) envelopes are transformed into aspherical bipolar/multipolar morphologies (Sahai & Trauger [7], Sahai, Morris & Villar [8]). Several mechanisms may explain the formation of the jet engines that produce such outflows and produce bipolar/multipolar structure in PPNe (Phillips & Ramos-Larios [9] and references therein), the most popular amongst these being common-envelope evolution (CEE) in close binary systems.

Binarity may also be responsible for the rapid and unexpected evolution of the Boomerang Nebula, which shows bipolar morphology similar to post-AGB PPNe (Wegener & Glass [10]; Sahai & Nyman [11]). However, the luminosity of the central star in the Boomerang is much lower ( $L \sim 300 \text{ L}_\odot$ ) than is possible for a post-AGB star. Sahai et al. [12] showed that the Boomerang is most likely a post-RGB star and that a merger with a binary companion may have triggered its extreme mass loss ( $\sim 10^{-3} \text{ M}_\odot \text{ yr}^{-1}$ ) at a very high ejection velocity ( $165 \text{ km s}^{-1}$ ), over a relatively short period (3500 yr) via CEE.

Kamath et al. [13–15] identified a group of stars in the LMC/SMC that are of too low a luminosity ( $<2500 L_{\odot}$ ) to be post-AGB, and rather these appear to be a new class of post-RGB objects. Further, they determined the properties of this class of objects. These objects show large mid-IR excess.

Optical spectroscopy allowed determination of their stellar parameters ( $T_{\text{eff}}$ ,  $\log g$ , [Fe/H] and E[B–V]). Using optical and *Spitzer* photometry, they integrated the spectral-energy-distributions (SEDs) to constrain the bolometric flux of the stars. The distance modulus for the LMC/18.54 mag and SMC/18.93 mag (Keller & Wood [16]) enabled reliable luminosity estimates. The Boomerang, with its mid-infrared excess and low luminosity, appears to be a Milky Way analog.

## 2. Sample Selection

We selected a sample of eight post-RGB stars in the LMC with mid and far-IR excess from Kamath et al. [14], hereafter KWW15. Our sample consists of an equal number of “shell” and “disk” sources. KWW15 introduced this classification based on a visual inspection of their dust SEDs.

The “shell” sources show far-IR excess and the peak of the dust emission lies beyond 10  $\mu\text{m}$ . The “disk” sources show near-IR excess indicative of hot dust and the peak of the dust SED lies around 10  $\mu\text{m}$  or sometimes even bluer. Further, on a color-color plot, the “shell” sources have  $[3.6]–[4.5] < 0.5$  and  $[8]–[24] > 4.0$ . Disk sources, on the other hand, have  $[3.6]–[4.5] > 0.5$ , or in some cases,  $[3.6]–[4.5] < 0.5$  in combination with  $[8]–[24] < 3.0$ . Additionally, to ensure that the objects are indeed post-RGB (and not post-AGB), we selected objects with  $L < 1000 L_{\odot}$ .

In order to investigate if the properties of the ejecta (e.g., mass, mass-loss rate, temperature, disk-to-shell mass ratio) are different between post-RGB and post-AGB stars, we also selected a sample of post-AGB LMC stars from KWW15, equally divided between “shell” and “disk” types. Our post-AGB stars are common between KWW15 and van Aarle et al. [17], the only exception being J051906.86-694153.9. This star showed the BaII line at 4554.03  $\text{\AA}$  (KWW15). The presence of BaII indicates a s-process enriched post-AGB object.

For many of the sources, KWW15 obtained vastly different values for the observed and photospheric luminosities. Their observed luminosity is obtained by integrating the flux under the observed SED. In the event of circumstellar dust and reddening, the former may be significantly less than the actual luminosity. Their derived photospheric luminosity depends on the extinction correction applied to the observed V-magnitude. KWW15’s formalism attempts to account for both interstellar and circumstellar reddening. If the V-magnitude is over-corrected, they would derive a higher luminosity for the object.

The photometry of the objects in this study was compiled by KWW15 and is available online from the Vizier database (<https://vizier.u-strasbg.fr/viz-bin/VizieR>, accessed on 31 January 2022) The photometric magnitudes were corrected for the combined effects of Galactic and LMC reddening using a mean  $E(B–V) = 0.08$  (Keller & Wood [16]). From the ultraviolet to the near-infrared, we used the LMC’s average extinction curve and  $R_v = 3.41$  as derived by Gordon et al. [18]. In the mid-infrared, we applied the extinction law by Gao et al. [19]. The observed SEDs extend from the U-band to 24  $\mu\text{m}$ .

## 3. Modeling the Circumstellar Dust

The SEDs were modeled using the one-dimensional radiative transfer code, DUSTY (Ivezić et al. [20]). DUSTY allows six different grain types: ‘warm’ and ‘cold’ silicates (Sil-Ow and Sil-Oc) from Ossenkopf et al. [21], silicate and graphite grains (Sil-DL and grf-DL) from Draine and Lee [22], amorphous carbon (amC-Hn) from Hanner [23] and silicon carbide (SiC-Pg) from Pégourié [24]. For our models, the dust grain composition was specified to be “warm” (Sil-Ow) silicates.

When the Sil-Ow grain composition did not provide a good fit, we tested different grain compositions. We used the Mathis, Rumpl and Nordsieck, MRN [25] grain size ( $a$ ) distribution function,  $n(a) \propto a^{-q}$  for  $a_{\min} \leq a \leq a_{\max}$ . DUSTY allows one to use

standard MRN parameters ( $q = 3.5$ ,  $a_{\min} = 0.005 \mu\text{m}$  and  $a_{\max} = 0.25 \mu\text{m}$ ) or modified MRN parameters. Whenever required, we used a modified MRN distribution by altering  $a_{\min}$  and  $a_{\max}$ . The dust density was assumed to be proportional to  $r^{-2}$ , where  $r$  is the radial distance from the star.

There are multiple input parameters associated with the dusty circumstellar environment that affect the SED, our strategy for exploring the parameter space is as follows. We first attempted to fit the SED using a single shell (one-component model), varying the dust temperature on the inner shell boundary ( $T_d$ ), the relative shell thickness ( $Y$  = ratio of the outer to the inner shell radius), the optical depth ( $\tau$ ) at  $0.55 \mu\text{m}$  and the grain-size distribution for a choice of grain composition.

If systematic discrepancies remained between the fit and the data, we then attempted a two-component fit, in which we added an inner component, representative of a hot, compact disk and varied its  $T_d$ ,  $Y$ ,  $\tau$ , and dust-grain properties. Specific wavelength ranges of the SED are relatively more sensitive to the shell and disk and help us to constrain their properties in a non-degenerate manner.

For the two-component fit (inner disk + outer shell), we approximated the inner disk by a spherical shell that intercepts a fraction of the direct starlight; e.g., as in Sahai et al. [26,27]. Such a shell is thus roughly equivalent to an axially-symmetric wedge-shaped fraction of a sphere; this fraction is hereafter referred to as the "disk fraction" and is presented in Tables 1 and 2. Thus, a disk with an opening angle of  $\theta_d$  is approximated by a shell that intercepts a fraction,  $\sin(\theta_d/2)$  of the radiation emitted within a  $4\pi$  solid angle, and the corresponding "disk-fraction" is  $\sin(\theta_d/2)$ . An illustration of the circumstellar geometry is provided in Figure 1.

A correctly illuminated model of the outer shell is then constructed assuming the shell to be divided into two parts. The fraction of the shell that lies in the shadow of the disk (=the disk-fraction) is illuminated by star light attenuated by the disk, together with the sum of the scattered and thermal emission from the disk within that fraction. The remaining fraction of the shell is illuminated by direct starlight plus the remaining fraction of the sum of scattered and thermal emission from the disk. The DUSTY code is run separately for each of the two parts of the outer shell and the outputs are added proportionately to obtain the final SED.

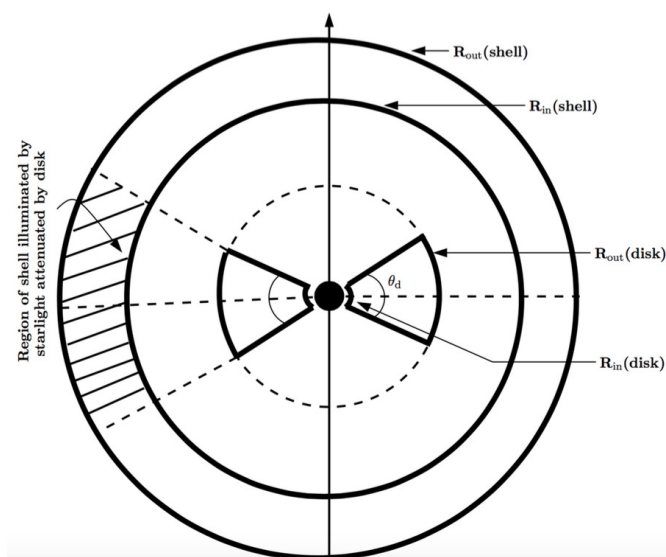


**Figure 1.** Illustration showing circumstellar dust geometry with an inner disk and an outer shell.  $R_{\text{in}}$  and  $R_{\text{out}}$  are the inner and outer radius of the disk (shell). A disk with an opening angle  $\theta_d$  intercepts  $\sin(\theta_d/2)$  (referred to as disk-fraction in this paper) of starlight.

**Table 1.** Important parameters derived from the best-fit post-RGB models.

Object	Disk-Fraction	Inner Disk							Outer Shell							L <sup>g</sup> (L <sub>⊕</sub> )
		Dust Grain Composition	T <sub>d</sub> <sup>a</sup> (in) (K)	τ <sup>b</sup>	a <sub>min</sub> <sup>c</sup> (μm)	a <sub>max</sub> <sup>d</sup> (μm)	Y <sup>e</sup>	M <sub>d</sub> <sup>f</sup> (M <sub>⊕</sub> )	Dust Grain Composition	T <sub>d</sub> <sup>a</sup> (in) (K)	τ <sup>b</sup>	a <sub>min</sub> <sup>c</sup> (μm)	a <sub>max</sub> <sup>d</sup> (μm)	Y <sup>e</sup>	M <sub>d</sub> <sup>f</sup> (M <sub>⊕</sub> )	
shell sources																
J043919.30-685733.4	0.35	Sil-Ow /1.0	1000	0.5	0.005	0.25	1.4	1.09 × 10 <sup>-10</sup>	Sil-Ow/1.0	130	0.65	0.005	0.25	20	2.60 × 10 <sup>-5</sup>	116
J051347.57-704450.5	...	...	...	...	...	...	...	...	Sil-Ow/1.0	250	0.35	0.1	0.25	3.0	2.00 × 10 <sup>-7</sup>	776
J051920.18-722522.1	0.4	Sil-Ow/1.0	500	0.4	0.3	20	2.0	1.29 × 10 <sup>-7</sup>	Sil-Ow/1.0	110	0.65	0.005	0.25	20	1.72 × 10 <sup>-4</sup>	582
J053930.60-702248.5	...	...	...	...	...	...	...	...	Sil-Ow/1.0	300	0.70	0.005	0.25	10	2.90 × 10 <sup>-7</sup>	295
disk sources																
J045555.15-712112.3	0.1	grf-DL/1.0	800	0.7	0.005	0.25	5.0	1.33 × 10 <sup>-8</sup>	Sil-Ow/0.8 + grf-DL/0.2	500	1.8	0.005	0.25	2.0	4.36 × 10 <sup>-7</sup>	621
J045755.05-681649.2	0.4	Sil-Ow/1.0	1300	0.5	0.005	2.0	2.0	4.82 × 10 <sup>-11</sup>	Sil-Ow/1.0	400	0.6	0.1	1.0	30.0	2.86 × 10 <sup>-7</sup>	217
J050257.89-665306.3	0.4	Sil-Ow/1.0	1200	0.5	0.3	5.0	3.0	2.88 × 10 <sup>-10</sup>	Sil-Ow/1.0	250	0.75	0.005	1.0	10.0	1.34 × 10 <sup>-6</sup>	303
J055102.44-685639.1	0.3	amC-Hn/1.0	2000	1.0	0.005	0.05	7.0	9.95 × 10 <sup>-11</sup>	Sil-Ow/0.4+SiC-Pg/0.6	350	12.0	0.005	0.07	3.0	1.52 × 10 <sup>-5</sup>	621

*a:* The (input) dust temperature at shell (disk) inner radius; *b:* The dust shell's (disk's) optical depth at 0.55 μm; *c:* The minimum dust grain size; *d:* The maximum dust grain size; *e:* The thickness of the disk/shell; *f:* The circumstellar dust mass; *g:* The (inferred) luminosity. The acronyms for the dust grain compositions refer to ‘warm’ silicates (Sil-Ow) from Ossenkopf et al. [21], graphite grains (grf-DL) from Draine and Lee [22], amorphous carbon (amC-Hn) from Hanner [23] and silicon carbide (SiC-Pg) from Pégourié [24].

**Table 2.** Important parameters derived from the best-fit post-AGB models.

Object	Disk-Fraction	Inner Disk							Outer Shell							L <sup>g</sup> (L <sub>⊕</sub> )
		Dust Grain Composition	T <sub>d</sub> <sup>a</sup> (in) (K)	τ <sup>b</sup>	a <sub>min</sub> <sup>c</sup> (μm)	a <sub>max</sub> <sup>d</sup> (μm)	Y <sup>e</sup>	M <sub>d</sub> <sup>f</sup> (M <sub>⊕</sub> )	Dust Grain Composition	T <sub>d</sub> <sup>a</sup> (in) (K)	τ <sup>b</sup>	a <sub>min</sub> <sup>c</sup> (μm)	a <sub>max</sub> <sup>d</sup> (μm)	Y <sup>e</sup>	M <sub>d</sub> <sup>f</sup> (M <sub>⊕</sub> )	
shell sources																
J050632.10-714229.8	...	grf-DL /0.3+Sil-Ow/0.7	350	0.4	0.1	1.0	5.0	3.75 × 10 <sup>-6</sup>	Sil-Ow/1.0	100	0.35	0.005	0.25	2.0	2.96 × 10 <sup>-4</sup>	5434
J051848.84-700247.0	...	...	...	...	...	...	...	...	Sil-Ow/1.0	350	3.2	0.005	0.25	20.0	8.80 × 10 <sup>-5</sup>	6210
J051906.86-694153.9	...	amC-Hn/1.0	2000	0.35	0.005	0.25	2.0	4.79 × 10 <sup>-11</sup>	SiC-Pg/1.0	160	0.07	2.3	3.0	2.0	8.90 × 10 <sup>-7</sup>	2018
J053250.69-713925.8	...	...	...	...	...	...	...	..	Sil-Ow/1.0	250	0.7	0.005	0.07	10.0	1.67 × 10 <sup>-4</sup>	4657
disk sources																
J045623.21-692749.0	...	Sil-Ow/1.0	1100	0.6	0.005	5.0	3.0	1.69 × 10 <sup>-8</sup>	Sil-Ow/1.0	150	0.1	0.005	0.25	2.0	4.12 × 10 <sup>-6</sup>	6598
J051418.09-691234.9	0.25	amC-Hn/1.0	1100	5.0	0.005	2.0	15.0	2.33 × 10 <sup>-7</sup>	Sil-Ow/0.4+grf-DL/0.6	600	0.4	0.005	0.25	30.0	6.05 × 10 <sup>-6</sup>	7763
J055122.52-695351.4	...	...	...	...	...	...	...	...	Sil-Ow/1.0	450	0.78	0.05	0.3	6.0	5.90 × 10 <sup>-6</sup>	4116
J052519.48-705410.0	0.35	Sil-Ow/1.0	800	1.0	0.005	0.25	20.0	1.82 × 10 <sup>-7</sup>	grf-DL/1.0	625	0.7	0.005	1.5	2.0	4.15 × 10 <sup>-7</sup>	3804

*a:* The (input) dust temperature at the shell (disk) inner radius. *b:* The dust shell's (disk's) optical depth at 0.55 μm. *c:* The minimum dust grain size. *d:* The maximum dust grain size. *e:* The thickness of the disk/shell. *f:* The circumstellar dust mass. *g:* The (inferred) luminosity. The acronyms for the dust grain compositions refer to ‘warm’ silicates (Sil-Ow) from Ossenkopf et al. [21], graphite grains (grf-DL) from Draine and Lee [22], amorphous carbon (amC-Hn) from Hanner [23] and silicon carbide (SiC-Pg) from Pégourié [24].

In some post-AGB stars, the SEDs may be a result of an interaction between a slow-moving cool outer shell ejected during the previous AGB phase and a fast-moving warm inner shell ejected during the post-AGB phase similar to the case of IRAS 22036+5306 (Sahai et al. [27]). Thus, a fit to the SED of the post-AGB stars J050632.10-714229.8, J051906.86-694153.9 and J045623.21-692749.0 was obtained assuming a pair of nested shells, i.e., a warm inner shell covering  $4\pi$  solid angle and a cool outer shell.

We arrived at the best-fit models, Figures 2 and 3 based on visual inspection of the observed and modeled data. In doing so, we gave more importance to matching the photometry at longer wavelengths ( $\lambda \gtrsim 2 \mu\text{m}$ ) as these are much less affected by the relatively uncertain intervening interstellar absorption along the line-of-sight to each object and potential stellar variability in the optical and near-infrared.

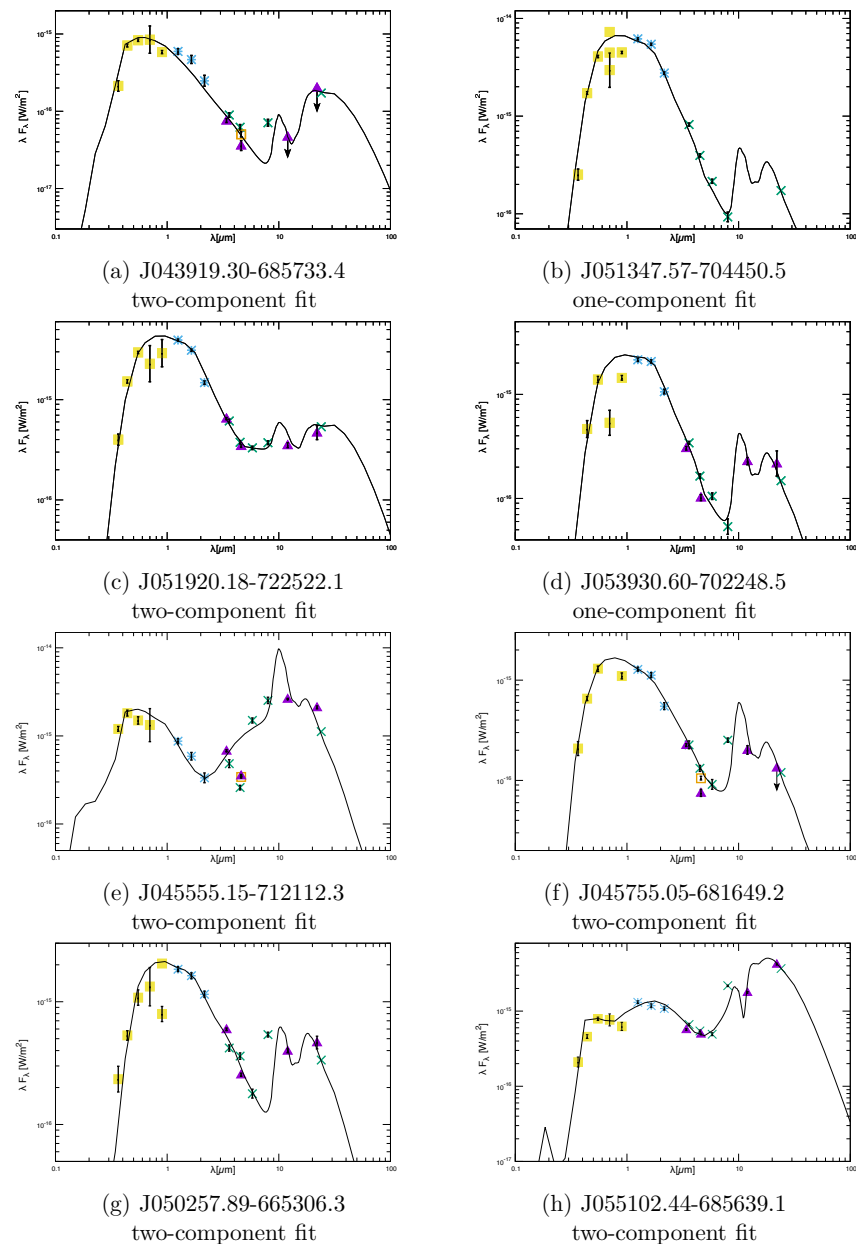


**Figure 2.** The best-fit models (black curves) to the observed SEDs of the post-RGB sources. The observed fluxes are de-reddened for Galactic and LMC reddening. U, B, V, R, I (yellow), 2MASS J, H and K (cyan) data are plotted along with WISE (purple) and ALLWISE (orange) photometry and data from the SAGE-LMC Survey (green), which covers the IRAC and MIPS bands. The error bars and upper limits (arrows) are indicated in black.

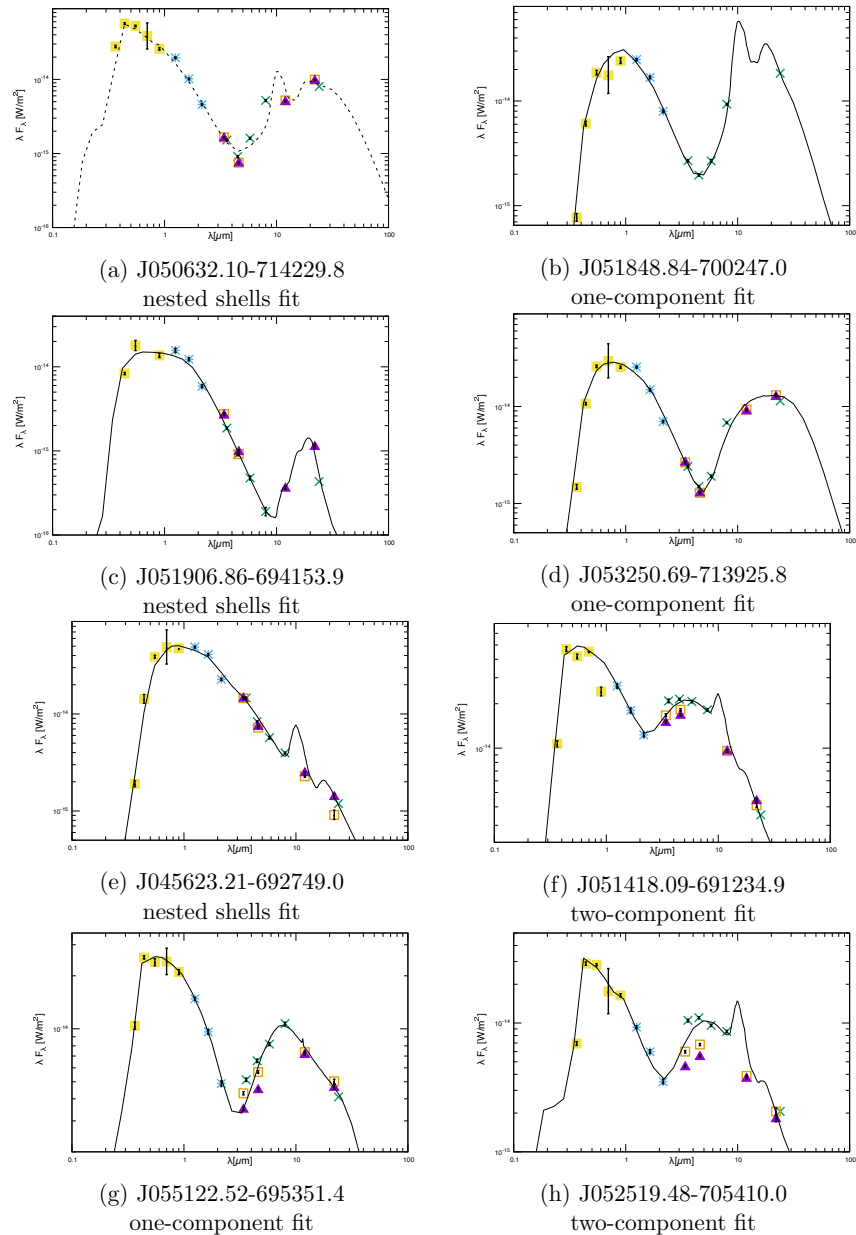


**Figure 3.** The best-fit models (black curves) to the observed SEDs of the post-AGB sources. The observed fluxes are de-reddened for Galactic and LMC reddening. U, B, V, R, I (yellow), 2MASS J, H and K (cyan) data are plotted along with WISE (purple) and ALLWISE (orange) photometry and data from the SAGE-LMC Survey (green), which covers the IRAC and MIPS bands. The error bars and upper limits (arrows) are indicated in black.

For sources where visual inspection could not discern between models, we used the reduced chi-square,  $\chi^2 = \sum \left( \frac{O_i - M_i}{\sigma_i} \right)^2 / (N - p - 1)$  to decide the best-fit model; where  $O_i$  is the observed flux,  $M_i$  is the model flux,  $\sigma_i$  is the error in the observed flux and  $N - p - 1$  is the number of degrees of freedom, with  $N$  equal to the number of observed datapoints and  $p$  equal to the number of free parameters (=5 for single shell models and 10 for two-component models).

#### 4. Derived Parameters

The DUSTY code outputs the SED, normalized to the bolometric flux,  $F_{\text{bol}}$ . We determined  $F_{\text{bol}}$  by scaling the model SED to match the de-reddened SED of our sources. The luminosity and dust mass ( $M_d$ ) in the circumstellar component was computed for each model. The distance to the LMC is  $d = 50$  kpc. We estimated the luminosity for each model as  $L = 4\pi d^2 F_{\text{bol}}$ .

For objects obeying a  $r^{-2}$  density distribution, the dust mass in the circumstellar component is given by,  $M_d = 4\pi R_{\text{in}}^2 Y(\tau_{100}/\kappa_{100})$  and the total mass (gas+dust),  $M_{\text{gd}}$  is approximately equal to the gas mass,  $M_d \delta$  for  $\delta >> 1$  (see Sarkar & Sahai [28]). Here,  $R_{\text{in}}$  is the inner radius of the dust shell inferred from the output of the DUSTY code,  $Y$  is the shell relative thickness specified in the DUSTY input ( $R_{\text{out}}/R_{\text{in}}$ ),  $\tau_{100}$  is the shell optical depth at 100  $\mu\text{m}$ ,  $\kappa_{100}$  is the dust mass absorption coefficient at 100  $\mu\text{m}$  and  $\delta$  is the gas-to-dust ratio. As in Sarkar & Sahai [28], we assume  $\kappa_{100} = 34 \text{ cm}^2 \text{g}^{-1}$  and  $\delta = 200$ .

The dust mass depends on the assumed gas-to-dust ratio. Considering that RGB stars are much less luminous than their AGB counterparts, the gas-to-dust ratio may deviate from the typical value of 200 for the post-AGBs. The dust composition around post-RGBs may be different from that around the post-AGBs. The gas-to-dust ratio may also depend on the metallicity of the galaxy, e.g., van Loon et al. [29]; Nanni et al. [30]. van Loon et al. [29] used a value of 500 for the LMC. Roman-Duval et al. [31] found gas-to-dust ratios of  $380^{+250}_{-130}$  in the LMC. Determining the gas-to-dust ratio as a function of fundamental stellar parameters (e.g., luminosity and metallicity) and evolutionary phase is still a distant goal (Sahai [32]). A higher value of  $\delta$  would imply a proportionate increase in the masses of the ejecta (dust and gas) that we derive for our sample of stars.

The dust mass absorption coefficient ( $\kappa$ ) is poorly constrained. This may be different for warm ( $\gtrsim 300$  K) and cold dust ( $\lesssim 300$  K) (e.g., Demyk [33]).  $\kappa$  also differs with wavelength. Its value at near-IR wavelengths where the bulk of the emission from an inner disk would occur is also not known. We uniformly used  $\kappa$  at 100  $\mu\text{m}$  for the cool and warm dust.

The derived parameters from our best-fit models are summarized in Tables 1 and 2. For our sample of post-RGB objects, the values of dust mass ( $M_d$ ) lie in the range  $3 \times 10^{-7} M_{\odot}$ – $1 \times 10^{-4} M_{\odot}$ . Lü et al. [34] discussed dust formation in the common envelope (CE) ejecta of binary systems wherein the giant is on the RGB (they call it the first giant branch or FGB), and the companion is a  $1 M_{\odot}$  degenerate star. Figure 4 shows our model dust mass values,  $M_d$ (outer shell) overplotted on Figure 2 of Lü et al. [34]. In Lü et al.'s models, the mass of dust produced in the CE ejecta of giants with masses  $1$ – $7 M_{\odot}$  ranges from about  $10^{-9} M_{\odot}$  to  $10^{-2} M_{\odot}$ . The lower end of this mass range corresponds to CEE occurring at the base of the RGB and the model parameter  $\gamma = 0.2$  (see eqn. 2 of Lü et al. [34] for a definition of  $\gamma$ ). Higher values of  $\gamma$  result in CE ejecta with relatively higher densities and thus more efficient dust formation. Thus, the upper end of the ejecta mass range corresponds to CEE occurring anywhere between the base and the tip of the RGB with  $\gamma \geq 0.3$  or at the tip of the RGB with  $\gamma \geq 0.2$ .

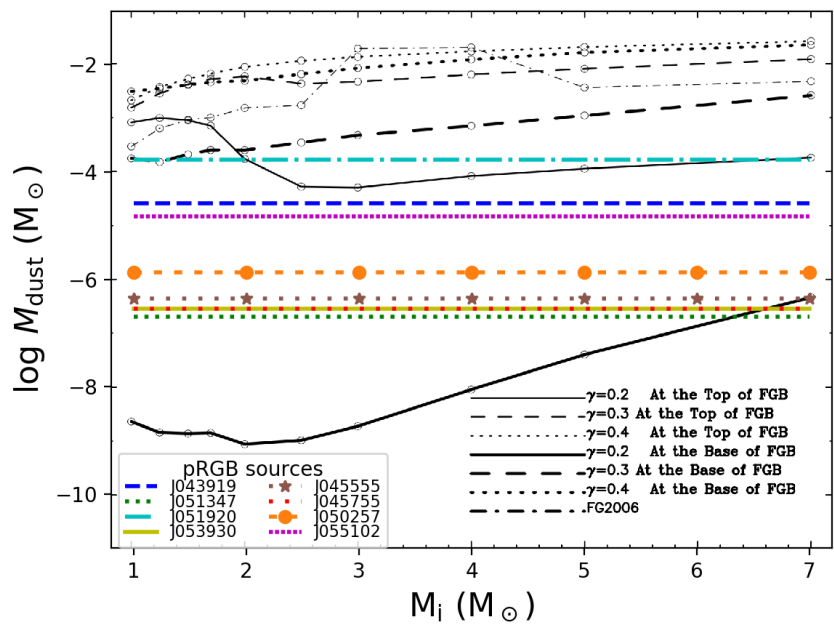


**Figure 4.** The dust mass in the outer shell of our post-RGB objects,  $M_d$  (Table 1) are shown (horizontal lines) on a plot of theoretically estimated dust masses in the ejecta of common envelope systems versus initial stellar mass, taken from Figure 2 of Lü et al. [34]. FGB refers to the first red giant branch. FG2006 refers to results by Ferrarotti & Gail [35], showing the dust masses produced in the dust-driven outflows of AGB stars.

## 5. Results

We modeled the SEDs of a select sample of post-RGB and post-AGB objects (eight in each class) in the LMC. Our main conclusions are listed below:

- We found that the published classification of these objects as “shell” or “disk” sources was not robust. While shells were present in all sources, our modeling showed that, additionally, the presence of a disk was (a) required in some “shell” sources (the post-RGB sources: J043919.30-685733.4 and J051920.18-722522.1) and (b) not required in some “disk” sources (the post-AGB sources: J045623.21-692749.0 and J055122.52-695351.4).
- With the exception of the post-RGB source, J045555.15-712112.3, the disk fractions in the post-RGBs were surprisingly large (typically 0.3–0.4), implying disks with large opening angles ( $\sim 41^\circ \pm 6^\circ$ ) and hence were geometrically thick structures. The large opening angles appeared to be roughly consistent with the gas density of the ejected envelope as seen in numerical simulations of CEE, relatively soon after CEE occurred (e.g., see Figure 1 of García-Segura et al. [36]).
- We derived the total dust mass in the disks and shells and set rough constraints on the dust grain composition and sizes. The shells are significantly more massive than the disks. The dust mass in the disks of post-RGB (post-AGB) sources lies in the range of  $5 \times 10^{-11}$ – $1 \times 10^{-7} M_\odot$  ( $5 \times 10^{-11}$ – $4 \times 10^{-6} M_\odot$ ) and in the shells from  $3 \times 10^{-7}$ – $1 \times 10^{-4} M_\odot$  ( $4 \times 10^{-7}$ – $3 \times 10^{-4} M_\odot$ ).
- We found evidence that, for some post-RGB sources, the ejected matter may be carbon-rich, even though it is expected to be oxygen-rich. For the post-RGB star, J055102.44-685639.1, our modeling revealed that the disk is optically thick ( $\tau = 1.0$ ) and amC-Hn grains provided a reasonable fit to the SED in the near and mid-infrared. The cool outer shell has a combination of warm silicates and silicon carbide. While amorphous carbon has been observed in the dusty disk around C-rich post-AGB stars (e.g., HR4049, Acke et al. [37]), we do not expect to see it in the circumstellar environment of a post-RGB star because such dust is believed to form when the C/O ratio is  $>1$  in the star’s atmosphere, following formation of C via  $3-\alpha$  nucleosynthesis and (the third) dredge-up—events that occur at the centers of AGB stars. The carbon-rich circumstellar

chemistry may be explained if the post-RGB star is a CH giant in a binary system that formed when the post-RGB progenitor accreted carbon-rich matter from a more massive AGB companion (now a WD) before undergoing CE ejection.

- We found systematic discrepancies between the model and observed SEDs in the 5.8–8  $\mu\text{m}$  region for some of our sources—J043919.30-685733.4, J045555.15-712112, J045755.05-681649.2, J050257.89-665306.3 and J050632.10-714229.8. These discrepancies may be explained by the presence of PAHs in the dust disks/shells of our sources, e.g., PAH molecules have been found in the circumstellar environment of the oxygen-rich red giant, HD233517 (Jura et al. [38]). The presence of PAHs provides independent support for the hypothesis of binary interaction leading to the formation of post-RGB objects.
- The amorphous silicate emission features at 10  $\mu\text{m}$  and 18  $\mu\text{m}$  are visible in the model spectra of several of our objects.
- Comparison of our model results with predictions of dust mass in the circumstellar ejecta of binary systems wherein the primary is a red giant suggests that CE ejection occurred near or at the tip of the RGB.

## 6. Discussion

Our study shows that post-RGB stars have large mid-infrared excesses resulting from the presence of dusty disks and shells. The extreme mass loss required for the infrared excess may be a consequence of CE interaction in binary systems as seen, e.g., in certain AGB stars in the LMC (Dell’Agli et al. [39]). These may be the result of standard CE ejection due to a rapid plunge in of the companion (Paczynski [40]) or a slow inspiral phase (Ivanova et al. [41], Podsiadlowski et al. [42], Ivanova et al., 2013 [43], Clayton et al. [44]).

An alternate scenario to these, proposed recently by Glanz & Perets [45], is that, during the inspiral phase, the CE expands to a very large radius, thus, allowing dust condensation and the formation of a dust-driven wind that evaporates the CE. Some fraction of the ejected mass may fall back and interact with the binary leading to the formation of circumbinary disks (Kashi & Soker [46]).

Dust formation in CE ejecta wherein the primary is a RGB star was studied by Lü et al. [34] and Iaconi et al. [47]. Lü et al. [34] were pessimistic about the difficulty of observing the dust produced in CE ejecta, since “the distance of dust formation in the CE ejecta is between  $\sim 10^{14}$  and  $10^{18}$  cm and is relatively far away from the FGB star”; however our study showed that dust is relatively easily detected in post-RGB sources between radii of few  $\times 10^{14}$  and  $10^{18}$  cm.

**Author Contributions:** Conceptualization, R.S.; methodology, R.S. and G.S.; software, G.S.; validation, R.S. and G.S.; formal analysis, G.S. and R.S.; writing—original draft preparation, G.S.; writing—review and editing, R.S and G.S. All authors have read and agreed to the published version of the manuscript.

**Funding:** G.S.’s contribution was funded by a DST grant, numbered SR/WOS-A/PM-93/2017. R.S.’s contribution to this research was funded in part by NASA via ADAP awards and multiple HST GO awards from the Space Telescope Science Institute.

**Data Availability Statement:** This research made use of the VizieR catalogue access tool, CDS, Strasbourg, France (doi:10.26093/cds/vizier). The original description of the VizieR service was published in 2000, A&AS 143, 23.

**Acknowledgments:** R.S.’s contribution to the research described here was conducted at the Jet Propulsion Laboratory, California Institute of Technology under a contract with NASA.

**Conflicts of Interest:** The authors declare no conflict of interest.

## References

- Bujarrabal, V.; Alcolea, J.; Sahai, R.; Zamorano, J.; Zijlstra, A.A. The shock structure in the protoplanetary nebula M1–92: Imaging of atomic and H<sub>2</sub> line emission. *Astron. Astrophys.* **1998**, *331*, 361–371.
- García-Lario, P.; Riera, A.; Manchado, A. Optical and Infrared Observations of the Bipolar Proto-Planetary Nebula Henize 401. *Astrophys. J.* **1999**, *526*, 854–861. [[CrossRef](#)]
- Hrivnak, B.J.; Smith, N.; Su, K.Y.L.; Sahai, R. A Study of H<sub>2</sub> Emission in Three Bipolar Proto-Planetary Nebulae: IRAS 16594–4656, Hen 3–401, and Rob 22. *Astrophys. J.* **2008**, *688*, 327–343. [[CrossRef](#)]
- Kwok, S.; Su, K.Y.L.; Hrivnak, B.J. Hubble Space Telescope V-Band Imaging of the Bipolar Proto-Planetary Nebula IRAS 17150–3224. *Astrophys. J.* **1998**, *501*, L117–L121 [[CrossRef](#)]
- Kwok, S.; Hrivnak, B.J.; Su, K.Y.L. Discovery of a Disk-collimated Bipolar Outflow in the Proto-Planetary Nebula IRAS 17106–3046. *Astrophys. J.* **2000**, *544*, L149–L152. [[CrossRef](#)]
- Sahai, R.; Trauger, J.T.; Watson, A.M.; Stapelfeldt, K.R.; Hester, J.J.; Burrows, C.J.; Ballister, G.E.; Clarke, J.T.; Crisp, D.; Evans, R.W.; et al. Imaging of the EGG Nebula (CRL 2688) with WFPC2/HST: A History of AGB/Post–AGB Giant Branch Mass Loss. *Astrophys. J.* **1998**, *493*, 301–311. [[CrossRef](#)]
- Sahai, R.; Trauger, J.T. Multipolar Bubbles and Jets in Low-Excitation Planetary Nebulae: Toward a New Understanding of the Formation and Shaping of Planetary Nebulae. *Astron. J.* **1998**, *116*, 1357–1366. [[CrossRef](#)]
- Sahai, R.; Morris, M.R.; Villar, G.G. Young Planetary Nebulae: Hubble Space Telescope Imaging and a New Morphological Classification System. *Astron. J.* **2011**, *141*, 134–164. [[CrossRef](#)]
- Phillips, J.P.; Ramos-Larios, G. Spitzer mid-infrared observations of seven bipolar planetary nebulae. *Mon. Not. R. Astron. Soc.* **2010**, *405*, 2179–2205. [[CrossRef](#)]
- Wegner, G.; Glass, I.S. A new bipolar nebula in Centaurus. *Mon. Not. R. Astron. Soc.* **1979**, *188*, 327–330. [[CrossRef](#)]
- Sahai, R.; Nyman, L.-A. The Boomerang Nebula: The Coldest Region of the Universe? *Astrophys. J.* **1997**, *487*, L155–L159. [[CrossRef](#)]
- Sahai, R.; Vlemmings, W.H.T.; Nyman, L.A. The Coldest Place in the Universe: Probing the Ultra-cold Outflow and Dusty Disk in the Boomerang Nebula. *Astrophys. J.* **2017**, *841*, 110–125. [[CrossRef](#)]
- Kamath, D.; Wood, P.R.; Van Winckel, H. Optically visible post-AGB/RGB stars and young stellar objects in the Small Magellanic Cloud: Candidate selection, spectral energy distributions and spectroscopic examination. *Mon. Not. R. Astron. Soc.* **2014**, *439*, 2211–2270. [[CrossRef](#)]
- Kamath, D.; Wood, P.R.; Van Winckel, H. Optically visible post-AGB stars, post-RGB stars and young stellar objects in the Large Magellanic Cloud. *Mon. Not. R. Astron. Soc.* **2015**, *454*, 1468–1502. [[CrossRef](#)]
- Kamath, D.; Wood, P.R.; Van Winckel, H.; Nie, J.D. A newly discovered stellar type: Dusty post-red giant branch stars in the Magellanic Clouds. *Astron. Astrophys.* **2016**, *586*, L5–L9. [[CrossRef](#)]
- Keller, S.C.; Wood, P.R. Bump Cepheids in the Magellanic Clouds: Metallicities, the Distances to the LMC and SMC, and the Pulsation-Evolution Mass Discrepancy. *Astrophys. J.* **2006**, *642*, 834–841. [[CrossRef](#)]
- Van Aarle, E.; Van Winckel, H.; Lloyd Evans, T.; Ueta, T.; Wood, P.R.; Ginsburg, A.G. The optically bright post-AGB population of the LMC. *Astron. Astrophys.* **2011**, *530*, 90–134. [[CrossRef](#)]
- Gordon, K.D.; Clayton, G.C.; Misselt, K.A.; Landolt, A.U.; Wolff, M.J. A quantitative comparison of the Small Magellanic Cloud, Large Magellanic Cloud, and Milky Way ultraviolet to near-Infrared extinction curves. *Astrophys. J.* **2003**, *594*, 279–293. [[CrossRef](#)]
- Gao, J.; Jiang, B.W.; Li, A.; Xue, M.Y. The mid-infrared extinction law in the Large Magellanic Cloud. *Astrophys. J.* **2013**, *776*, 7–19. [[CrossRef](#)]
- Ivezic, Z.; Nenkova, M.; Heymann, F.; Elitzur, M. User Manual for DUSTY (V4). 2012. Available online: <https://github.com/ivezic/dusty> (accessed on 31 January 2022).
- Ossenkopf, V.; Henning, T.; Mathis, J. Constraints on cosmic silicates. *Astron. Astrophys.* **1992**, *261*, 567–578.
- Draine, B.T.; Lee, H.M. Optical properties of interstellar graphite and silicate grains. *Astrophys. J.* **1984**, *285*, 89–98. [[CrossRef](#)]
- Hanner, M.S. Infrared Observations of Comets Halley and Wilson and Properties of the Grains. *NASA Conf. Pub.* **1988**, *3004*, 22.
- Pégourié, B. Optical properties of alpha silicon carbide. *Astron. Astrophys.* **1988**, *194*, 335–339.
- Mathis, J.S.; Rumpl, W.; Nordsieck, K.H. The size distribution of interstellar grains. *Astrophys. J.* **1977**, *217*, 425–433. [[CrossRef](#)]
- Sahai, R.; Zijlstra, A.; Sánchez Contreras, C.; Morris, M. An Icy, Bipolar Proto-Planetary Nebula with Knotty Jets: IRAS 22036+5306. *Astrophys. J.* **2003**, *586*, L81–L85. [[CrossRef](#)]
- Sahai, R.; Young, K.; Patel, N.A.; Sánchez Contreras, C.; Morris, M. A massive bipolar outflow and a dusty torus with large grains in the preplanetary nebula IRAS 22036+5306. *Astrophys. J.* **2006**, *653*, 1241–1252. [[CrossRef](#)]
- Sarkar, G.; Sahai, R. The Dust Envelope of the Preplanetary Nebula IRAS 19475+3119. *Astrophys. J.* **2006**, *644*, 1171–1182. [[CrossRef](#)]
- Van Loon, J.T.; Groenewegen, M.A.T.; de Koter, A.; Trams, N.R.; Waters, L.B.F.M.; Zijlstra, A.A.; Loup, C. Mass-loss rates and luminosity functions of dust-enshrouded AGB stars and red supergiants in the LMC. *Astron. Astrophys.* **1999**, *351*, 559–572.
- Nanni, A.; Groenewegen, M.A.T.; Aringer, B.; Rubele, S.; Bressan, A.; van Loon, J.T.; Goldman, S.R.; Boyer, M.L. The mass-loss, expansion velocities, and dust production rates of carbon stars in the Magellanic Clouds. *Mon. Not. R. Astron. Soc.* **2019**, *487*, 502–521. [[CrossRef](#)]

31. Roman-Duval, J.; Gordon, K.D.; Meixner, M.; Bot, C.; Bolatto, A.; Hughes, A.; Wong, T.; Babler, B.; Bernard, J.P.; Clayton, G.C.; et al. Dust and gas in the Magellanic Clouds from the HERITAGE Herschel Key Project. II. Gas-to-dust ratio variations across Interstellar medium phases. *Astrophys. J.* **2014**, *797*, 86–109. [[CrossRef](#)]
32. Sahai, R. *Astro2010: The Astronomy and Astrophysics Decadal Survey*; Science White Papers, No. 256; NASA: Washington, DC, USA, 2009.
33. Demyk, K.; Meny, C.; Leroux, H.; Depecker, C.; Brubach, J.-B.; Roy, P.; Nayral, C.; Ojo, W.-S.; Delpech, F. Low-temperature MIR to submillimeter mass absorption coefficient of interstellar dust analogues. II. Mg and Fe-rich amorphous silicates. *Astron. Astrophys.* **2017**, *606*, 50–62. [[CrossRef](#)]
34. Lü, G.; Zhu, C.; Podsiadlowski, P. Dust Formation in the Ejecta of Common Envelope Systems. *Astrophys. J.* **2013**, *768*, 193–199. [[CrossRef](#)]
35. Ferrarotti, A.S.; Gail, H. Composition and quantities of dust produced by AGB-stars and returned to the interstellar medium. *Astron. Astrophys.* **2006**, *447*, 553–576. [[CrossRef](#)]
36. García-Segura, G.; Ricker, P.M.; Taam, R.E. Common Envelope Shaping of Planetary Nebulae. *Astrophys. J.* **2018**, *860*, 19–32. [[CrossRef](#)]
37. Acke, B.; Degroote, P.; Lombaert, R.; De Vries, B.L.; Smolders, K.; Verhoelst, T.; Lagadec, E.; Gielen, C.; Van Winckel, H.; Waelkens, C. Amorphous carbon in the disk around the post-AGB binary HR 4049. Discerning dust species with featureless opacity curves. *Astron. Astrophys.* **2013**, *551*, 76–90. [[CrossRef](#)]
38. Jura, M.; Bohac, C.J.; Sargent, B.; Forrest, W.J.; Green, J.; Watson, D.M.; Sloan, G.C.; Markwick-Kemper, F.; Chen, C.H.; Najita, J. Polycyclic Aromatic Hydrocarbons orbiting HD 233517, an evolved oxygen-rich red giant. *Astrophys. J.* **2006**, *637*, L45–L48. [[CrossRef](#)]
39. Dell’Agli, F.; Marini, E.; D’Antona, F.; Ventura, P.; Groenewegen, M.A.T.; Mattsson, L.; Kamath, D.; García-Hernández, D.A.; Tailo, M. Are extreme asymptotic giant branch stars post-common envelope binaries? *Mon. Not. R. Astron. Soc.* **2021**, *502*, L35–L39. [[CrossRef](#)]
40. Paczynski, B. Structure and Evolution of Close Binary Systems. In *IAU Symp. 73*; Eggleton, P., Mitton, S., Whelan, J., Eds.; Kluwer Academic Publishers: Dordrecht, The Netherlands, 1976; p. 75.
41. Ivanova, N.; Podsiadlowski, P.; Spruit, H. Hydrodynamical simulations of the stream–core interaction in the slow merger of massive stars. *Mon. Not. R. Astron. Soc.* **2002**, *334*, 819–832. [[CrossRef](#)]
42. Podsiadlowski, P.; Ivanova, N.; Justham, S.; Rappaport, S. Explosive common-envelope ejection: Implications for gamma-ray bursts and low-mass black-hole binaries. *Mon. Not. R. Astron. Soc.* **2010**, *406*, 840–847 [[CrossRef](#)]
43. Ivanova, N.; Justham, S.; Chen, X.; De Marco, O.; Fryer, C.L.; Gaburov, E.; Ge, H.; Glebbeek, E.; Han, Z.; Li, X.-D.; et al. Common envelope evolution: Where we stand and how we can move forward. *Astron. Astrophys. Rev.* **2013**, *21*, 59–141. [[CrossRef](#)]
44. Clayton, M.; Podsiadlowski, P.; Ivanova, N.; Justham, S. Episodic mass ejections from common-envelope objects. *Mon. Not. R. Astron. Soc.* **2017**, *470*, 1788–1808. [[CrossRef](#)]
45. Glanz, H.; Perets, H.B. Efficient common-envelope ejection through dust-driven winds. *Mon. Not. R. Astron. Soc.* **2018**, *478*, L12–L17. [[CrossRef](#)]
46. Kashi, A.; Soker, N. A circumbinary disc in the final stages of common envelope and the core-degenerate scenario for Type Ia supernovae. *Mon. Not. R. Astron. Soc.* **2011**, *417*, 1466. [[CrossRef](#)]
47. Iaconi, R.; Maeda, K.; Nozawa, T.; De Marco, O.; Reichardt, T. Properties of the post in-spiral common envelope ejecta II: Dust formation. *Mon. Not. R. Astron. Soc.* **2020**, *497*, 3166. [[CrossRef](#)]